Journal of Biomedical Materials Research Part A

WILEY

Society For Biomaterials

RESEARCH ARTICLE OPEN ACCESS

Zinc Oxide@Tetracycline Spiky Microparticles Design for Persistent Antibacterial Therapy

Youjin Seol[1,2] | Keya Ganguly[1,3] | Tejal V. Patil[1,2] | Sayan Deb Dutta[1,4] | Hyeonseo Park[1,2] | Jieun Lee[1,2] | Aayushi Randhawa[1,2] | Hojin Kim[1,2] | Ki-Taek Lim[1,2,4]

[1]Department of Biosystems Engineering, Kangwon University, Chuncheon, Gangwon-do, Republic of Korea | [2]Interdisciplinary Program in Smart Agriculture, Kangwon National University, Chuncheon, Gangwon-do, Republic of Korea | [3]Department of Mechanical Engineering, Virginia Tech, Blacksburg, Virginia, USA | [4]Institute of Forest Science, Kangwon National University, Chuncheon, Gangwon-do, Republic of Korea

Correspondence: Ki-Taek Lim (ktlim@kangwon.ac.kr)

Received: 19 January 2025 | **Revised:** 21 March 2025 | **Accepted:** 8 April 2025

Funding: This work was supported by the Innovative Human Resource Development for Local Intellectualization program through the Institute of Information & Communications Technology Planning & Evaluation (IITP) grant funded by the Korean government (MSIT) (IITP-2025-RS-2023-00260267) and Basic Science Research Program through the National Research Foundation of Korea(NRF) funded by the Ministry of Education (RS-2022-NR075661).

Keywords: antibiotic resistance | biomimetic | rupture | spike microparticle | tetracycline beads

ABSTRACT

Antibiotics have revolutionized medical treatment by effectively combating bacterial infections, particularly those associated with chronic wounds and implant complications. Nevertheless, the persistent use of these drugs has resulted in an increase in antibiotic-resistant bacteria and biofilm infections, highlighting the urgent need for alternative therapies. This study presents an approach for combating persistent bacterial and biofilm infections through the integration of biomimetic design and advanced nanotechnology. Inspired by the natural defense mechanisms of pollen grains and lotus leaves, we engineered zinc oxide spiky microparticles combined with tetracycline-loaded beads mimicking the structure of lotus leaf papillae. This biomimetic design exhibits a multifaceted antimicrobial strategy, leveraging hierarchical micro/nanostructures and the inherent antibacterial properties of their natural counterparts. ZnO microparticles, which mimic the morphology of pollen grains, provide topological cues to rupture adhered bacteria, whereas tetracycline beads, inspired by lotus leaf papillae, deliver a controlled release of antibiotics to target persistent bacteria. Using a synergistic multimodal approach, our biomimetic materials demonstrated exceptional efficacy in eradicating persistent methicillin-resistant *Staphylococcus aureus* and *Escherichia coli* infections, offering promising prospects for the development of advanced antibacterial therapies. This study not only underscores the importance of biomimicry in material design but also highlights the potential of integrating nature-inspired strategies with nanotechnology for biomedical applications.

1 | Introduction

Persistent bacterial infections and biofilms pose a considerable healthcare challenge [1, 2]. Biofilms are aggregated communities of bacteria embedded within a self-generated extracellular polymeric substance (EPS) matrix. The matrix is composed of polysaccharides, proteins, lipids, DNA, and other biopolymers and protects encapsulated bacterial colonies [3]. These biofilms can attach to diverse substrates such as living tissues and medical devices. They are highly tolerant to physical and

---

Youjin Seol and Keya Ganguly contributed equally to this study.

https://doi.org/10.1002/jbm.a.37915

chemical stressors and pose a major threat to human health. Biofilms that adhere to the surfaces of medical devices cause Healthcare-associated infections, including urinary tract infections and pneumonia linked to ventilator use, and implant-related infections, which significantly increase mortality [4, 5]. Biofilm infections can also have deleterious effects. For instance, biofilms in the cystic fibrosis lung cause chronic infection and reduce life expectancy to 35–50 years [6]. Biofilms are present in 78.2% of chronic wounds [7], and global treatment costs are estimated at $281 billion [8]. Biofilms not only shield bacteria from external toxins but the extracellular polymeric substance also significantly diminishes antibiotic efficacy [5–7]. This complexity increases because biofilms are not homogeneous cultures of physiologically similar cells; various mechanisms protect subpopulations of cells within the biofilm [9]. These mechanisms include antibiotic failure to penetrate biofilms, slow growth rates in nutrient-deficient zones resulting in dormant cells that may develop antibiotic resistance, and differential metabolism (low and high), leading to antibiotic failure against processes in actively growing bacteria, such as replication, transcription, translation, and cell wall synthesis. Thus, biofilm bacteria with low metabolic activity located in the inner region of the biofilm exhibit enhanced antimicrobial tolerance. Other considerations include persistent cells (drug-resistant bacteria), hypoxia (which may impair multidrug function), and the extracellular biofilm matrix charge (which can function as an ion-exchange resin, binding to various charged antibiotics) [10]. Consequently, treatment outcomes are compromised, further escalating healthcare costs [11], especially because of the repeated use of expensive broad-spectrum antibiotics, such as amoxicillin, ciprofloxacin, cephalexin, chloramphenicol, doxycycline, and tetracycline(TC) [12, 13]. In addition, ZnO has garnered interest because of its superior antibacterial activity compared with that of other nanomaterials [14]. The primary antibacterial action of ZnO involves the generation of reactive oxygen species (ROS) [15]. Redox reactions between oxygen and water on the surface of the ZnO particles lead to ROS formation [16]. ROS disrupt the chemical bonds in bacterial organic matter, leading to bactericidal effects. Hydroxyl radicals accumulate on the bacterial cell membrane, altering its structure, while hydrogen peroxide penetrates the membrane, damaging essential cellular components such as DNA and proteins, thereby enhancing bactericidal activity [16].

TC is a low-cost and commonly used broad-spectrum antibiotic, making it a practical choice for outpatient care in resource-constrained regions with restricted healthcare funding. This antibiotic has demonstrated activity against various gram-negative and gram-positive bacterial strains [17]. Furthermore, TC is cost-effective and generally well-tolerated, with few adverse effects [18, 19]. However, as a first-generation antibiotic, TC has limitations in combating antibiotic-resistant bacterial strains when used as a standalone treatment. Combination therapies are emerging, in which antibiotics are combined with a dispersal agent, such as nanoparticles [20]. In recent years, both organic and inorganic nanoparticles have been investigated as antimicrobial approaches to combat antimicrobial-resistant bacteria and biofilms [18, 19, 21]. Among these, ZnO stands out because of its low toxicity and biodegradability, which address the safety concerns associated with other nanoparticles [22].

Creative approaches like fabricating biomimetic and antibiofilm micro/nanocarriers are promising strategies for tackling this urgent problem [23, 24]. Among the various micro/nanocarriers, the complex physicochemical structures of pollen grains and lotus leaves have inspired the development of potent antibacterial agents [25–27]. The hierarchical micro/nanostructures of these microparticles provide distinct topological signals that disrupt bacterial cell membranes and adhesion, thereby reducing biofilm development and facilitating bacterial elimination [28]. Researchers are exploring the self-cleaning and antimicrobial properties of lotus leaves to develop surfaces that replicate these features, enhancing antibacterial effectiveness [23, 29]. Lotus leaf papillae are tiny protrusions coated with microscale wax crystals, creating a water-repellent surface that prevents bacterial adhesion, whereas high-aspect-ratio nanotubes mechanically rupture bacteria attached to leaves [26]. Using the lotus leaf papillae as inspiration, TC beads have been developed to provide sustained delivery [30]. However, studies have not combined the antibacterial topological effects of ZnO microparticles with controlled antibiotic release from lotus-leaf-inspired TC beads.

Our research integrated biomimetics and nanotechnology to develop spiky ZnO microparticles inspired by spiky pollen structures. These microparticles, with beaded TC attached to their spikes, mimic lotus leaf papillae for enhanced antibacterial effectiveness. Additionally, they address the issue of non-degradability by enabling the progressive breakdown of spikes in simulated body fluid. We employed a nature-inspired design to develop an innovative strategy to combat antibiotic-resistant bacteria and advance their biomedical applications. Figure 1 illustrates the synthesis process of the designed microparticles and their antimicrobial mechanism of action.

2 | Experimental Section

2.1 | Materials

Zinc nitrate hexahydrate (purity > 98%) and magnesium chloride were purchased from Thermo-Fisher Scientific (USA). Hydroxylamine hydrochloride (purity > 97%) was provided by Daejung, Republic of Korea. NaOH (98% purity) was purchased from Alfa Aesar (France). Potassium chloride and TC were purchased from Sigma–Aldrich. *Escherichia coli* (KCTC-2593, Republic of Korea) was obtained from the Korean Collection of Type Cultures. Methicillin-resistant *Staphylococcus aureus* (MRSA) was purchased from the American Type Culture Collection (Manassas, Virginia, USA).

2.2 | Synthesis of Pollen-Inspired ZnO (P-ZnO) and Lotus-Inspired TC ZnO (PT-ZnO)

P-ZnO particles that mimic pollen particles were synthesized using a simple one-pot method. P-ZnO particles were prepared using a previously published method with minor modifications

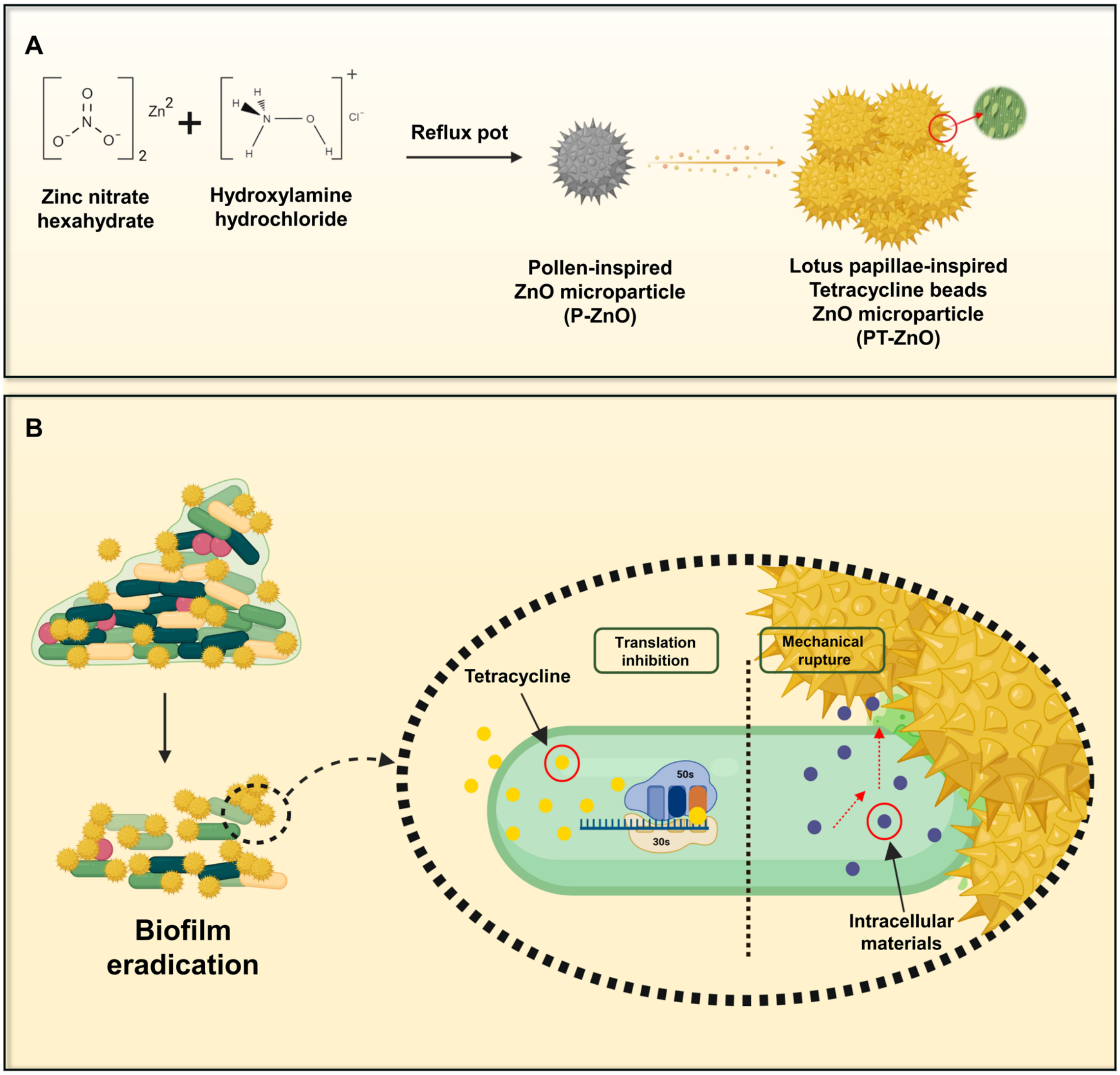

FIGURE 1 | Schematic diagram of the antibacterial mechanism of PT-ZnO for bacterial killing and biofilm eradication. (a) Diagram of the fabrication of P-ZnO and PT-ZnO. (b) Antimicrobial and antibiofilm mechanism of engineered microparticles.

[31]. A 0.3 M solution of zinc nitrate hexahydrate and 0.1 M of hydroxylamine hydrochloride was dissolved in 50 mL of distilled water. Subsequently, a 3 M sodium hydroxide solution in 50 mL of distilled water was prepared and poured into the zinc nitrate hexahydrate and hydroxylamine hydrochloride mixture while stirring. The pH of the mixture was adjusted to 12. After stirring for 30 min, the aqueous solution was transferred to a reflux port and calcined at 90°C for 20 min. It was then washed three times with methanol and dried at 40°C.

PT-ZnO particles were prepared following a previously reported method with minor modifications [32]. Briefly, ZnO microparticles (20 mg) were dispersed in 1 mL of a TC solution (10 mg/mL) prepared with Milli-Q water. The mixture was agitated for 24 h and centrifuged. It was then washed with Milli-Q water and dried at 40°C. The structures of P-ZnO and PT-ZnO were characterized using field-emission scanning electron microscopy (SEM) (JEOL JSM-7900F), X-ray photoelectron spectroscopy (Thermo VG (K Alpha), +), and Fourier transform infrared (FTIR) spectroscopy (Thermo Scientific (iN10/iS50)).

2.3 | In Vitro Drug Release Analysis

All release experiments were conducted in phosphate-buffered saline (PBS). PT-ZnO was prepared as a 1 mg/mL suspension in PBS and subsequently incubated at 37°C. Samples were obtained at designated time points (0, 30, 60, 180, and 300 min), centrifuged, and the absorbance of the supernatant was measured at 275 nm.

The amount of drug released was determined by comparing the absorbance at 275 nm with that of a 10 mg/mL TC solution in PBS [33]. The percentage of the drug released from PT-ZnO was calculated using the following formula:

$$\text{Drug release}\,(\%) = \frac{Drug\ release(mg)}{Drug\ loaded\ in\ NPs(at\ time = 0, mg)} \times 100$$

2.4 | Minimal Inhibitory Concentration (MIC)

The MIC was defined as the minimum concentration that inhibited visible bacterial growth, as determined using the agar medium dilution method. A 50 μL suspension of bacteria (*E. coli*, MRSA) was inoculated onto P-ZnO and PT-ZnO at varying concentrations (0.5, 1, 2, 3, and 4 mg/mL) and incubated at 37°C for 24 h. Subsequently, 100 μL of 10^{-5} serially diluted bacterial suspension was spread onto nutrient agar plates.

2.5 | Antibacterial and Antibiofilm Performance

MRSA and *E. coli* were isolated from agar plates and cultured overnight in Luria–Bertani broth. The bacterial concentration was determined by measuring optical density (OD) at 600 nm. Before beginning the experiment, the bacterial solution was diluted with medium until the OD reached 0.1. A volume of 80 μL of bacteria was introduced into 400 μLof P-ZnO or PT-ZnO liquid solution and incubated for 24 h. The group without the sample served as the control, whereas the group containing TC was designated as the positive control. The antibacterial efficacy was determined by measuring the OD (600 nm) of the bacterial culture after treatment. Following 24 h of incubation, 100 μL of 10^{-5} serially diluted bacteria were plated onto nutrient agar. After 24 h of incubation at 37°C, colonies were identified.

The bacterial survival rate was calculated using the following equation.

$$Bacterial\ survival\ rate(\%) = \left[\frac{absorbance\ of\ sample\ at\ 600nm}{absorbance\ of\ Contol\ at\ 600nm}\right] \times 100$$

Bacterial Live/dead bacterial cells were observed using SYTO 9 and propidium iodide (1 μL). Staining was carried out for 15 min after 24 h of treatment with P-ZnO (2 mg/mL) and PT-ZnO (0.5 mg/mL). A confocal laser scanning microscope (Leica, DMi8) was used to image the stained bacteria. Live bacteria exhibited green fluorescence, whereas dead bacteria exhibited red fluorescence. Images were obtained using SEM to confirm the bacterial killing mechanism of the spiked particles. After treatment with each nanoparticle for 1 h, the bacteria were collected by centrifugation at 10,000 rpm. After washing once with PBS, 4% paraformaldehyde was added and incubated at 4°C for 1 h to fix the bacteria. The cells were then dehydrated with 30%, 50%, 70%, 80%, 90%, and 100% EtOH. Three microliters of the dehydrated bacteria were dropped onto a cover glass, dried, and observed using SEM.

2.6 | Biofilm Assay

Bacteria (adjusted to OD 0.1) were added to each 24-well plate (1 mL) and cultured in a stationary state for 2 days. The medium was changed daily to allow mature biofilm formation. The biofilm was then washed once with PBS to eliminate any floating bacteria. The nanoparticles were applied and incubated for 24 h to determine their ability to remove biofilms.

To quantify the amount of biofilm, the biofilm was washed with PBS 24 h after the sample was added, followed by the application of 400 μL of 0.1% crystal violet solution and a 15 min incubation at room temperature. After the crystal violet was removed and the biofilm was rinsed again with PBS, it was dried in an oven at 40°C for 2 h and then observed under a microscope. The bound dye was subsequently dissolved in 33% acetic acid, and the absorbance of the resulting solution was measured at 590 nm.

2.7 | Quantitative RT-PCR for Bacterial Gene Expression

Total RNA and cDNA were extracted and synthesized using the Universal RNA Extraction Kit (TaKaRa, Japan,) PrimeScript 1st Strand cDNA Synthesis Kit (TaKaRa, Japan) according to the manufacturer's guidelines. The purity and concentration of the RNA and cDNA were determined using a spectrophotometer. Real-time PCR was performed using a Bio-Rad Real-Time PCR (system (CFX96TM) Maestro Real-Time system; Bio-Rad, USA). The cycling conditions were as follows: 1 cycle at 95°C for 3 min followed by 41 cycles at 95°C for 10 s and 65°C for 30 s. All experiments were conducted in triplicate and were referenced to the housekeeping gene 16S rRNA for normalization. The primer sequences for *16S rRNA*, *flu*, *gapA*, *aap*, *icaR*, *sarA*, and *agrA* are listed in Table S1.

2.8 | Statistical Analysis

Statistical analysis was performed using Origin Pro v9.1 (Origin Laboratories, U.S.A.) for all the experiments. The significant difference between the control and treatment groups was assessed using the one-way analysis of variance (ANOVA) test. Data reported in this study are mean ± SD of triplicate ($n = 3$) experiments, statistical significance at $*p \leq 0.05$, $**p \leq 0.01$, and $***p \leq 0.001$.

3 | Results and Discussion

3.1 | Characterization of P-ZnO and PT-ZnO Microparticles

The morphology and chemical properties of the fabricated microparticles were characterized. We observed a well-defined spiky array of spherical P-ZnO microparticles with a smooth surface (Figure 2a), having an average diameter of 2.68 μm (Figure 2b). By contrast, bead-like structures resembling lotus papillae were observed on the surface of the spiky PT-ZnO microparticles (Figure 2c), with an average diameter of 2.91 μm (Figure 2d). Additionally, P-ZnO and PT-ZnO microparticles exhibited gradual degradation over 7 days in simulated body fluid solution (Figure S1). Furthermore, SEM images of PT-ZnO particles at various time points after drug release showed that their spike-like structures remained intact over time (Figure S2).

The microparticle and hierarchical arrangement of nanotubes on the surface of lotus leaves endow them with defensive properties and remarkable super-hydrophobicity [26, 34, 35]. The experimental contact angle for PT-ZnO particles was 99.61°, indicating that they were hydrophobic and resembled the properties of lotus leaves (Figure S3). The spiky P-ZnO microparticles likely developed during our synthesis because of fast nucleation and anisotropic growth under high-pH conditions. Zinc nitrate and hydroxylamine hydrochloride generated Zn^{2+} and OH^- ions, while sodium hydroxide increased the pH to 12, promoting ZnO precipitation. The elevated pH and reflux at 90°C facilitated anisotropic growth

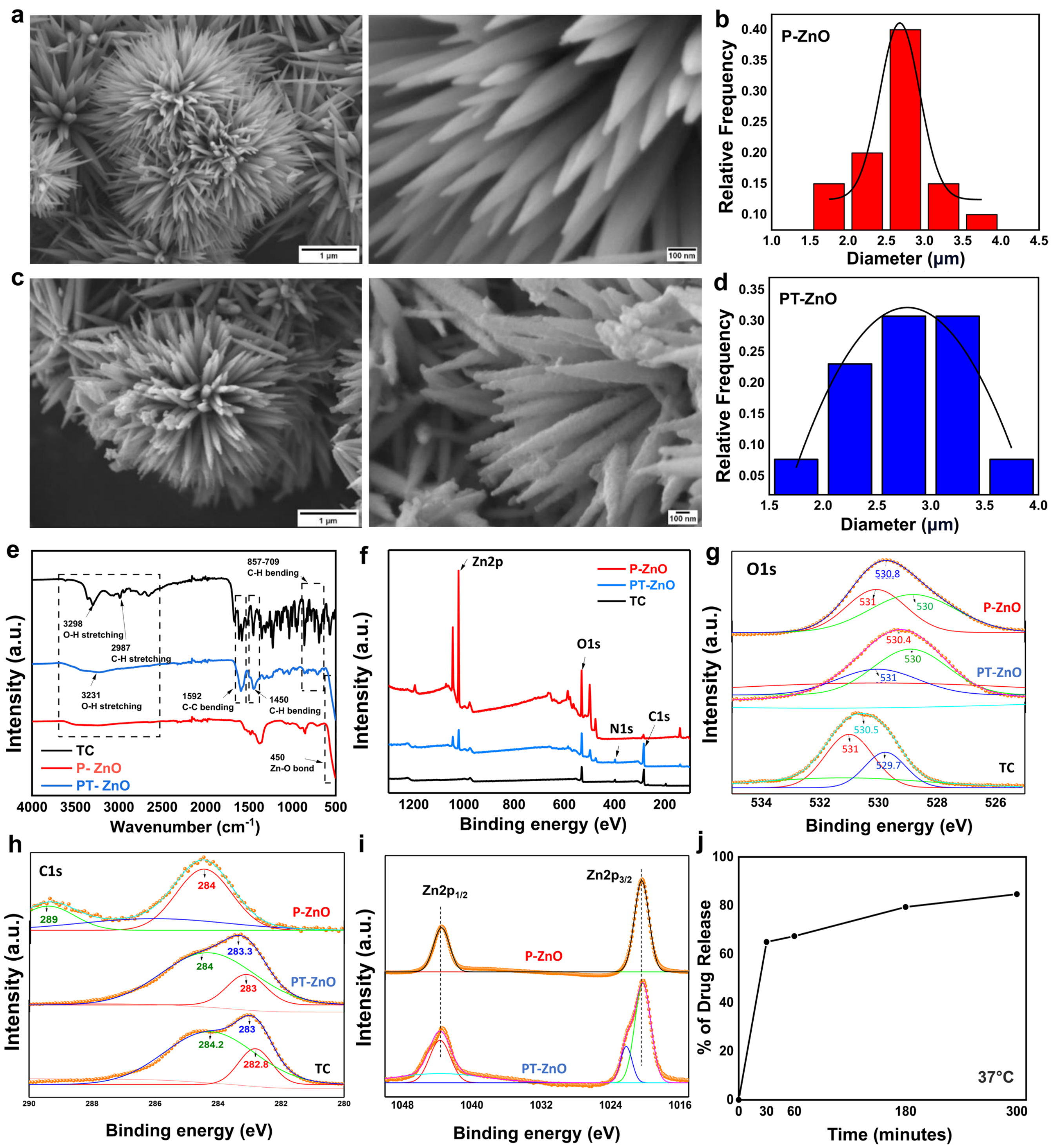

FIGURE 2 | Fabrication and chemical characterization of P-ZnO and PT-ZnO. SEM images of (a) P-ZnO and (c) PT-ZnO. Size distribution of (b) P-ZnO, (d) PT-ZnO. (e) FTIR spectra, (f) XPS wide and (g-i) narrow scan spectra. (j) In vitro release of tetracycline from PT-ZnO.

along the c-axis, leading to the formation of spiky structures. Hydroxylamine influenced surface chemistry, stabilized facets, and promoted directional growth. The reflux and calcination processes enhanced crystal formation, while washing and drying maintained a spiky, pollen-like shape [36–38]. The development of spiky PT-ZnO microparticles containing beaded TC was facilitated by the increased surface area and reactivity of the spiky ZnO configuration, which enhanced drug adsorption. Anisotropically grown ZnO microparticles contain several high-energy sites along their spikes, facilitating strong interactions with TC molecules that possess functional groups such as hydroxyl, amine, and keto groups. These groups interact with surface Zn^{2+} ions through electrostatic interactions, hydrogen bonding, or chelation, particularly near the spike tips, where local charge density is elevated. Throughout the 24h agitation process, TC molecules progressively adsorbed onto the spikes, forming bead-like clusters due to localized aggregation. Following centrifugation and washing procedures eliminate surplus, unbound TC while drying at 40°C guarantees the stable attachment of the adsorbed TC to the ZnO surface. The bead-like morphology of TC formed as it accumulated around the spikes, driven by its affinity for high-energy reactive sites on the spiky ZnO surface. The chemical compositions of the P-ZnO and PT-ZnO microparticles were examined using FTIR spectroscopy, and the results are presented in Figure 2e. The individual FTIR spectra of P-ZnO, TC, and PT-ZnO confirmed that the FTIR spectrum of PT-ZnO contained the characteristic peaks of both P-ZnO and TC, demonstrating the chemical interaction between TC and ZnO. The absorption peak at 450 cm^{-1} in the spectra of P-ZnO and PT-ZnO corresponds to Zn – O vibration, indicating zinc oxide production [39]. Additionally, the 1447 cm^{-1} peak in the PT-ZnO spectrum is attributed to C–H bending, indicating the presence of alkane groups. In the PT-ZnO spectrum, the bands observed at 1592 and 1098 cm^{-1} correspond to C=C stretching and C–O bending vibrations, respectively, confirming the incorporation of TC in PT-ZnO. Moreover, in the PT-ZnO spectrum, the peaks near 857, 823, and 709 cm^{-1} were found to be due to C–H vibrations, indicating the presence of TC in PT-ZnO. The nanostructures of TC, P-ZnO, and PT-ZnO were analyzed by XPS. In the TC and PT-ZnO spectra, an N1s peak was observed, which was absent in the P-ZnO spectrum (Figure 2f). The O1s spectra of P-ZnO and PT-ZnO were deconvoluted into three peaks as indicated in Figure 2g. The feature appearing at 530 eV with low energy is associated with the presence of O^{2-} ions in the wurtzite crystalline structure [40]. The mid-level and higher binding energy components at 530.6 and 531 eV are related to oxygen-deficient regions within the ZnO matrix [41]. Figure 2h shows that the spectra of both TC and PT-ZnO displayed C=C (peaks at 283 and 284 eV, respectively). The peaks at 1043 eV and 1020 eV in the PT-ZnO and P-ZnO samples, respectively, as depicted in Figure 2i, are assigned to Zn 2p$_{1/2}$ and Zn 2p$_{3/2}$ [42]. Consequently, the FTIR and XPS analyses confirmed that TC was effectively integrated with ZnO particles in PT-ZnO. The in vitro release of PT-ZnO in PBS was evaluated at various time points. An initial burst release of the drug from PT-ZnO was observed between 0 and 30 min, with most of the drug released after 5 h (Figure 2j).

3.2 | Antibacterial Performance of ZnO and TC-ZnO Microparticles

The antibacterial performance of P-ZnO and PT-ZnO was confirmed using *E. coli* and MRSA. The results are demonstrated in Figure 3. The concentrations of P-ZnO and PT-ZnO used in the antibacterial experiments were evaluated according to the MIC values, which were 2 mg/mL for *E. coli* and 0.5 mg/mL for MRSA. The agar plate results of MIC experiments against MRSA and *E. coli* are shown in Figure S4. As illustrated in Figure 3a, the bacterial survival rate following PT-ZnO treatment was 22% in *E. coli* and 14% in MRSA, the lowest among all groups ($p < 0.001$) (Figure 3a). In a plate culture count experiment, the TC and P-ZnO groups had fewer bacterial colonies than those in the control group. By contrast, the PT-ZnO group showed almost no colonies on the plates (Figure 3b). SYTO 9 is a highly effective green-fluorescent nuclear and chromosomal stain that can penetrate both prokaryotic and eukaryotic cell membranes. Conversely, propidium iodide, which binds to DNA, only stains dead cells by penetrating compromised cell membranes, causing a shift from green to red fluorescence [43]. Live/dead analyses revealed that both bacterial strains exhibited a high number of green fluorescent spots in the control group. By contrast, the TC, P-ZnO, and PT-ZnO groups showed a greater number of red fluorescent spots (Figure 3c). Spiked microparticles were observed in the TC group relative to those in the control group, whereas red fluorescent spots were predominantly observed in the P-ZnO and PT-ZnO groups. Notably, the PT-ZnO group exhibited the highest concentration of red fluorescence, highlighting the potent antibacterial effect of PT-ZnO. The SEM images revealed that bacterial cell membranes in the P-ZnO and PT-ZnO treatment groups were disrupted. By contrast, bacteria with intact cell membranes were observed in the control and TC groups (Figure 3d). These findings illustrate the mechanism by which spikes in P-ZnO and PT-ZnO particles exert mechanical stress on the bacterial membrane, leading to membrane rupture and leakage of intracellular components, ultimately causing bacterial cell death. Additionally, the zeta potential was measured to evaluate the influence of nanoparticle surface charge on the physical interaction mechanism. The measured zeta potentials of P-ZnO and PT-ZnO were − 11.9 mV and − 16.5 mV, respectively (Figure S5). Previously, cationic nanoparticles demonstrated better antibacterial effects than those of neutral or anionic nanoparticles [44–47]. However, both nanoparticles used in this study exhibited high antibacterial activity despite their negative charges. As confirmed by SEM images, the spike-shaped nanoparticles mechanically killed the bacterial cells by physically damaging the cell membrane. In addition, TC penetrated the captured bacteria, and the TC released from PT-ZnO bound to bacterial ribosomes, inhibiting protein synthesis [48], indicating a stronger antibacterial effect than that of P-ZnO. Thus, it was confirmed that the antibacterial mechanism of the nanoparticles developed in this study resulted primarily from a combination of physical interactions with the cell membrane via the spike structure and biochemical action of TC.

The bacterial survival rate experiments revealed that the PT-ZnO group exhibited a more pronounced antibacterial effect against MRSA than against *E. coli*. These results may be attributed to structural differences between gram-negative and gram-positive bacteria. Gram-negative bacteria have an outer membrane located outside the peptidoglycan layer. This outer membrane is selectively permeable, impeding the entry of antibiotics into bacterial cells [49, 50]. The surface charge properties of P-ZnO and PT-ZnO were assessed by zeta potential analysis.

3.3 | Effect of Microparticles on Biofilm Formation

We found an inhibitory effect of PT-ZnO on *E. coli* and MRSA biofilm formation, and the results are shown in Figure 4. Wounds containing biofilms impair the formation of the epidermis, dermis, and blood vessels, leading to chronic wounds and hindering the wound healing process [51]. Therefore, biofilm disruption is essential for promoting effective wound healing. We first evaluated the ability of P-ZnO and PT-ZnO to inhibit biofilm formation in *E. coli* and MRSA cultures using crystal violet staining (Figure 4a). Microscopic analysis revealed that both *E. coli* and MRSA appeared dark purple in the control group, indicating the presence of dense biofilms. However, a marked reduction in staining was observed in both P-ZnO and PT-ZnO groups, with the PT-ZnO group exhibiting the greatest

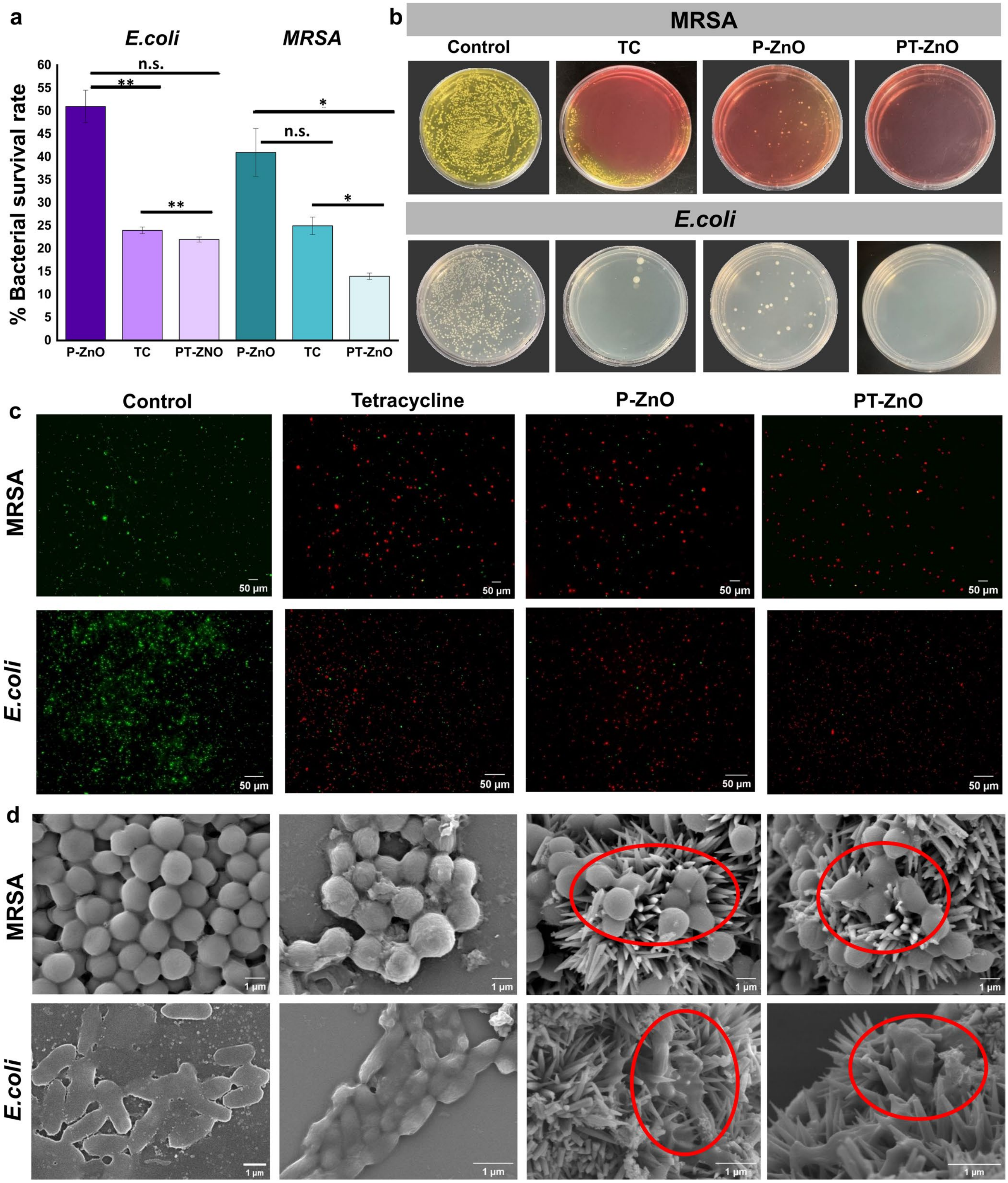

FIGURE 3 | Antibacterial properties of ZnO and TC-ZnO. (a) Bacterial survival rates. (b) Bacterial colonies on agar plates from different groups. (c) Live/dead staining. (d) SEM image of different groups. Statistical significance was calculated by one-way ANOVA using the Tukey post hoc ($^*p \leq 0.05$, $^{**}p \leq 0.01$, and $^{***}p \leq 0.001$).

reduction. The absorbance values of the groups are shown in Figure 4b,c. These findings suggest that PT-ZnO effectively inhibited biofilm formation by reducing the presence of bacteria and penetrating the microenvironment. We speculated that the mechanism by which the biofilm barrier is destroyed by PT-ZnO's spike structure involves TC penetration and bacterial cell membrane damage within the biofilm, resulting in biofilm removal.

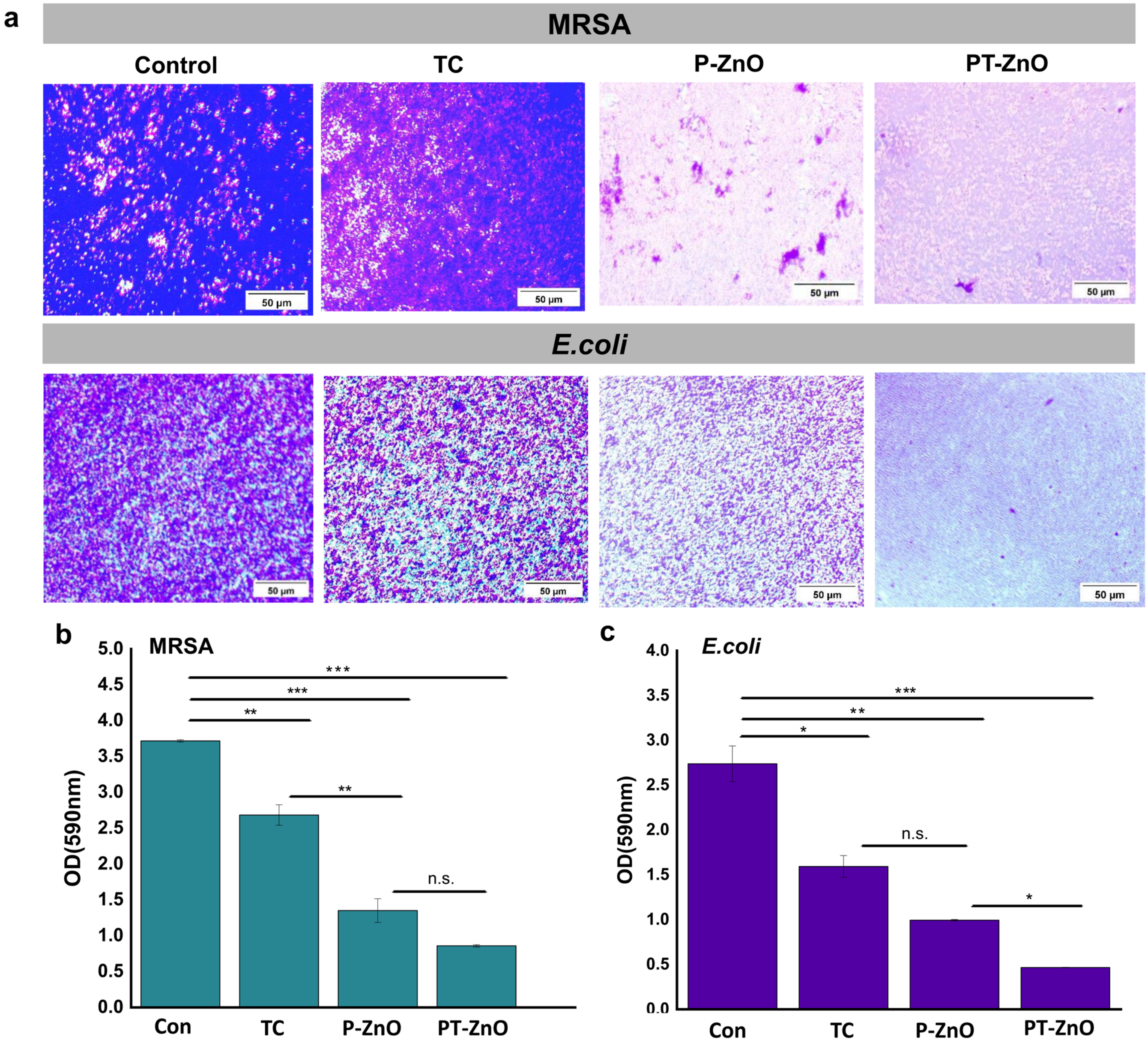

FIGURE 4 | Antibiofilm properties of ZnO and TC-ZnO. (a) Microscopy images of biofilms treated with samples stained with crystal violet and absorbance at 590 nm (b) MRSA (c) *E. coli*. Statistical significance was calculated by one-way ANOVA using the Tukey post hoc (*$p \le 0.05$, **$p \le 0.01$, and ***$p \le 0.001$).

3.4 | Effect of P-ZnO and PT-ZnO on the Expression Level of Biofilm-Related Genes

The expression levels of genes (*flu*, *gapA*, *icaR*, *sigB*, *agrA*, and *sarA*) related to biofilm formation and energy metabolism were evaluated using PCR (Figure 5). The *gapA* gene codes glyceraldehyde-3-phosphate dehydrogenase (GAPDH), a key enzyme involved in glycolysis, that plays a critical role in the metabolic pathway converting glucose into energy [52]. Since GAPDH is essential for ATP generation and supplies precursors for diverse biosynthetic processes, the expression level of *gapA* could indirectly affect biofilm formation capacity. The *flu* gene activates genes necessary for the synthesis of the extracellular matrix, which facilitates biofilm formation [53]. The *icaR* gene functions as a regulator by inhibiting the expression of *icaABCD*, thereby preventing biofilm formation [54, 55]. The *sigB* gene encodes an RNA polymerase sigma factor, and bacteria with a knockout phenotype exhibit impaired biofilm formation [56]. The *sarA* and *agrA* genes regulate the virulence gene network and play crucial roles in biofilm formation [57]. All genes related to biofilm formation were expressed at lower levels in the P-ZnO and PT-ZnO groups than in the control group after 24 h. Notably, the PT-ZnO group exhibited significantly low expression levels of all genes, ranging from 0.01 to 0.07 (Figure 5a–f). These findings indicate that PT-ZnO exerted an antibiofilm effect by downregulating the expression of genes specifically involved in biofilm development.

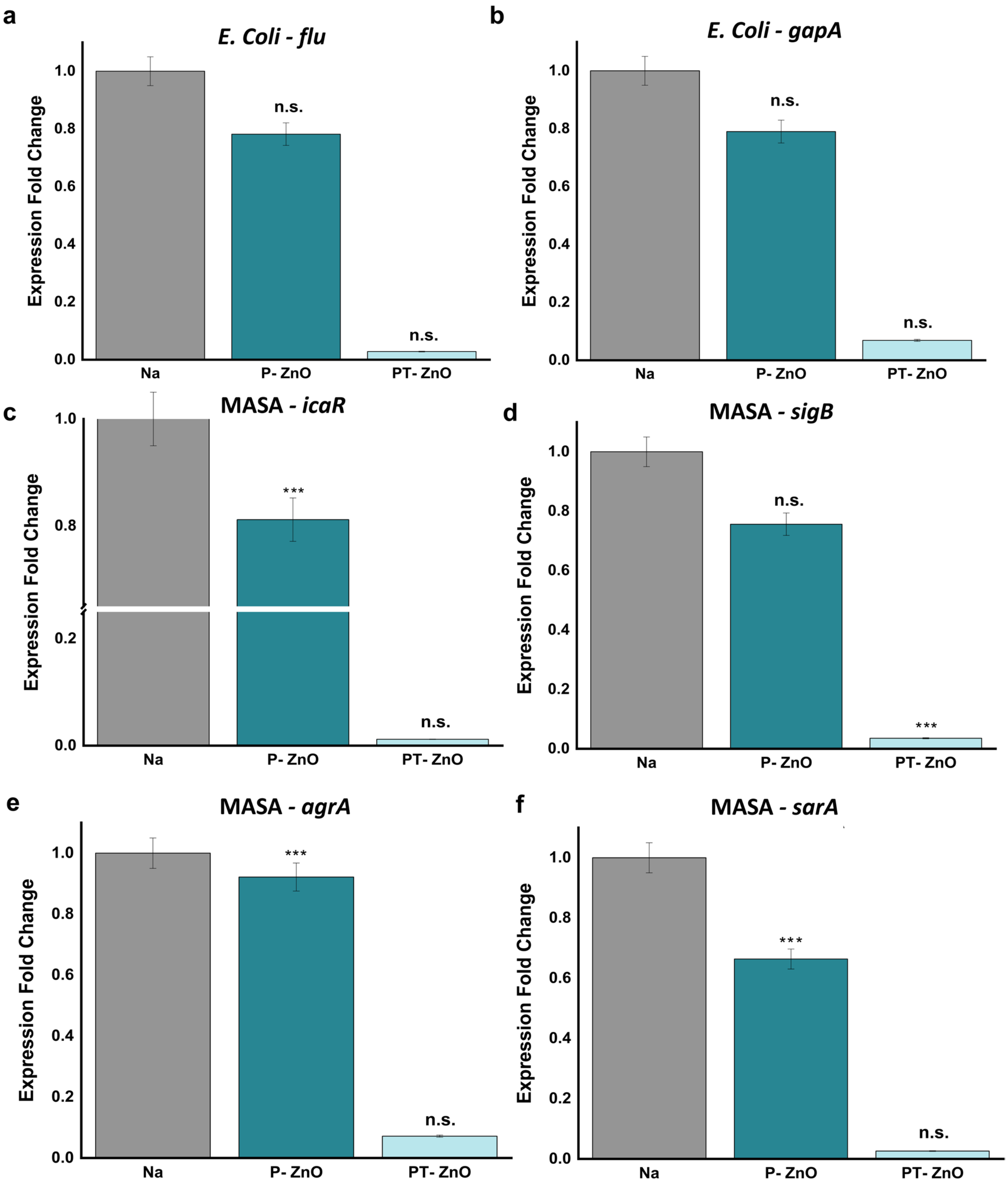

FIGURE 5 | *E. coli* and MRSA bacterial PCR results after 24 h. Expression of (a) *gapA*, (b) *aap*, (c) *icaR*, (d) *sigB*, (e) *agrA*, and (f) *sarA*. Statistical significance was calculated by one-way ANOVA using the Tukey post hoc (*$p \leq 0.05$, **$p \leq 0.01$, and ***$p \leq 0.001$).

3.5 | Discussion

The fabricated spike-like particles exhibit promising applications in diverse fields. For example, their distinctive structural characteristics regulate immune cell responses, accelerate wound healing [58], and exhibit a nanobridge effect that promotes skin adhesion and wound closure, effectively preventing prolonged blood and fluid loss [59, 60]. Moreover, PT-ZnO particles have great potential as surface materials for use in implants and wound dressings. Zinc oxide nanoparticles can penetrate bacteria through direct interaction with cell membranes [61]. ROS generated from Zn – O bonds damage membrane integrity and inactivate surface proteins, ultimately leading to cell death [62]. In addition, Zn^{2+} ions diffuse into the bacterial cytoplasm, inducing oxidative stress, inhibiting enzyme activity, promoting protein aggregation, and enhancing cell adhesion, contributing to the potent antibacterial properties of ZnO [63, 64].

Furthermore, spike-like particles influence cellular activities, including adhesion and protein adsorption, promoting wound healing [65]. However, this aspect requires refinement, as an overabundance of Zn^{2+} released from zinc oxide particles could result in cytotoxic effects [66].

4 | Conclusion

The development of antibacterial materials capable of combating diverse antibiotic-resistant bacteria is a pressing challenge. We designed spike-like nanoparticles inspired by the natural architecture of pollen grains and lotus leaves, tailored to combat antibiotic-resistant bacterial infections and biofilms. In this study, we successfully synthesized and characterized P-ZnO and PT-ZnO. The synthesized P-ZnO and PT-ZnO exhibited spike structures resembling pollen, whereas PT-ZnO featured TC beads shaped like lotus papillae. Additionally, we demonstrated that PT-ZnO exhibits remarkable antibacterial and antibiofilm activities against *E. coli* and MRSA. SEM images from bacterial experiments confirmed that PT-ZnO breached the bacterial cell membrane, leading to mechanical sterilization. PCR analysis of biofilm-related gene expression revealed that the PT-ZnO group exhibited significantly low expression of antibiofilm-related genes. This study illustrates that this approach is an effective strategy for addressing persistent bacterial and biofilm-associated infections.

Conflicts of Interest

The authors declare no conflicts of interest.

Data Availability Statement

The data that support the findings of this study are available on request from the corresponding author. The data are not publicly available due to privacy or ethical restrictions.

References

1. A. Singh, A. Amod, P. Pandey, et al., "Bacterial Biofilm Infections, Their Resistance to Antibiotics Therapy and Current Treatment Strategies," *Biomedical Materials* 17 (2022): 022003.

2. P. Bowler, C. Murphy, and R. Wolcott, "Biofilm Exacerbates Antibiotic Resistance: Is This a Current Oversight in Antimicrobial Stewardship?," *Antimicrobial Resistance & Infection Control* 9 (2020): 162.

3. H.-C. Flemming, J. Wingender, U. Szewzyk, P. Steinberg, S. A. Rice, and S. Kjelleberg, "Biofilms: An Emergent Form of Bacterial Life," *Nature Reviews Microbiology* 14 (2016): 563–575.

4. D. R. Dodds, "Antibiotic Resistance: A Current Epilogue," *Biochemical Pharmacology* 134 (2017): 139–146.

5. S. W. Lee, K. S. Phillips, H. Gu, M. Kazemzadeh-Narbat, and D. Ren, "How Microbes Read the Map: Effects of Implant Topography on Bacterial Adhesion and Biofilm Formation," *Biomaterials* 268 (2021): 120595.

6. M. Cámara, W. Green, C. E. MacPhee, et al., "Economic Significance of Biofilms: A Multidisciplinary and Cross-Sectoral Challenge," *NPJ Biofilms and Microbiomes* 8 (2022): 42.

7. M. Malone, T. Bjarnsholt, A. J. McBain, et al., "The Prevalence of Biofilms in Chronic Wounds: A Systematic Review and Meta-Analysis of Published Data," *Journal of Wound Care* 26 (2017): 20–25.

8. W.H.O. Global Spending on Health: A World in Transition, https://www.who.int/publications/i/item/WHO-HIS-HGF-HFWorkingPaper-19.4.

9. H. Y. Liu, E. L. Prentice, and M. A. Webber, "Mechanisms of Antimicrobial Resistance in Biofilms," *NPJ Antimicrobials and Resistance* 2 (2024): 27.

10. I. Olsen, "Biofilm-Specific Antibiotic Tolerance and Resistance," *European Journal of Clinical Microbiology & Infectious Diseases* 34 (2015): 877–886.

11. T.-F. Mah, B. Pitts, B. Pellock, G. C. Walker, P. S. Stewart, and G. A. O'Toole, "A Genetic Basis for Pseudomonas Aeruginosa Biofilm Antibiotic Resistance," *Nature* 426 (2003): 306–310.

12. G. M. Rossolini, F. Arena, P. Pecile, and S. Pollini, "Update on the Antibiotic Resistance Crisis," *Current Opinion in Pharmacology* 18 (2014): 56–60.

13. A. S. Grewal, A. K. Dhingra, K. Nepali, G. Deswal, and A. L. Srivastav, *Contemporary Approaches to Mitigating Antibacterial Drug Resistance* (IGI Global, 2024).

14. M. Alavi and A. Nokhodchi, "Synthesis and Modification of Bio-Derived Antibacterial ag and ZnO Nanoparticles by Plants, Fungi, and Bacteria," *Drug Discovery Today* 26 (2021): 1953–1962.

15. B. Abebe, E. A. Zereffa, A. Tadesse, and H. C. A. Murthy, "A Review on Enhancing the Antibacterial Activity of ZnO: Mechanisms and Microscopic Investigation," *Nanoscale Research Letters* 15 (2020): 190.

16. S. Jiang, K. Lin, and M. Cai, "ZnO Nanomaterials: Current Advancements in Antibacterial Mechanisms and Applications," *Frontiers in Chemistry* 8 (2020): 580.

17. R. Mukherjee, M. Patra, D. Dutta, M. Banik, and T. Basu, "Green Synthesized Cerium Oxide Nanoparticle: A Prospective Drug Against Oxidative arm," *Biochimica et Biophysica Acta (BBA) - General Subjects* 1860 (2016): 1929–1941.

18. S. Taghavi Fardood, F. Moradnia, S. Heidarzadeh, and A. Naghipour, "Green Synthesis Characterization Photocatalytic and Antibacterial Activities of Copper Oxide Nanoparticles of Copper Oxide Nanoparticles," *Nano Research* 8, no. 2 (2023): 134–140, https://doi.org/10.22036/ncr.2023.02.006.

19. N. Tripathi and M. K. Goshisht, "Recent Advances and Mechanistic Insights Into Antibacterial Activity, Antibiofilm Activity, and Cytotoxicity of Silver Nanoparticles," *ACS Applied Bio Materials* 5 (2022): 1391–1463.

20. F. Fatima, S. Siddiqui, and W. A. Khan, "Nanoparticles as Novel Emerging Therapeutic Antibacterial Agents in the Antibiotics Resistant Era," *Biological Trace Element Research* 199 (2021): 2552–2564.

21. A. Abdelghafar, N. Yousef, and M. Askoura, "Zinc Oxide Nanoparticles Reduce Biofilm Formation, Synergize Antibiotics Action and Attenuate Staphylococcus Aureus Virulence in Host; an Important Message to Clinicians," *BMC Microbiology* 22 (2022): 244.

22. B. Das, S. Moumita, S. Ghosh, et al., "Biosynthesis of Magnesium Oxide (MgO) Nanoflakes by Using Leaf Extract of Bauhinia Purpurea and Evaluation of Its Antibacterial Property Against Staphylococcus Aureus," *Materials Science and Engineering: C* 91 (2018): 436–444.

23. S. V. Oopath, A. Baji, M. Abtahi, T. Q. Luu, K. Vasilev, and V. K. Truong, "Nature-Inspired Biomimetic Surfaces for Controlling Bacterial Attachment and Biofilm Development," *Advanced Materials Interfaces* 10 (2023): 2201425.

24. K. Yang, J. Shi, L. Wang, et al., "Bacterial Anti-Adhesion Surface Design: Surface Patterning, Roughness and Wettability: A Review," *Journal of Materials Science and Technology* 99 (2022): 82–100.

25. J. A. Finbloom, C. Huynh, X. Huang, and T. A. Desai, "Bioinspired Nanotopographical Design of Drug Delivery Systems," *Nature Reviews Bioengineering* 1 (2023): 139–152.

26. R. Jiang, L. Hao, L. Song, et al., "Lotus-Leaf-Inspired Hierarchical Structured Surface With Non-Fouling and Mechanical Bactericidal Performances," *Chemical Engineering Journal* 398 (2020): 125609.

27. Y. Yang, B. Wang, Q. Liu, et al., "Sunflower Pollen-Derived Microcapsules Adsorb Light and Bacteria for Enhanced Antimicrobial Photothermal Therapy," *Nanoscale* 16, no. 17 (2024): 8378–8389, https://doi.org/10.1039/d3nr04814d.

28. M. Sun, K. F. Chan, Z. Zhang, et al., "Magnetic Microswarm and Fluoroscopy-Guided Platform for Biofilm Eradication in Biliary Stents," *Advanced Materials* 34 (2022): 2201888.

29. X. Ding and S. Mou, "Ion Chromatographic Analysis of Tetracyclines Using Polymeric Column and Acidic Eluent," *Journal of Chromatography A* 897 (2000): 205–214.

30. Z. Saadatidizaji, N. Sohrabi, R. Mohammadi, and M. S. Amini-Fazl, "Tetracycline Hydrochloride Loaded-Alginate Based Nanoparticle-Hydrogel Beads for Potential Wound Healing Applications: In Vitro Drug Delivery, Release Kinetics, and Antibacterial Activity," *International Journal of Biological Macromolecules* 264 (2024): 130653.

31. R. Wahab, N. K. Kaushik, A. K. Verma, et al., "Fabrication and Growth Mechanism of ZnO Nanostructures and Their Cytotoxic Effect on Human Brain Tumor U87, Cervical Cancer HeLa, and Normal HEK Cells," *JBIC Journal of Biological Inorganic Chemistry* 16 (2011): 431–442.

32. S. Das, K. Vishakha, S. Banerjee, D. Nag, and A. Ganguli, "Tetracycline-Loaded Magnesium Oxide Nanoparticles With a Potential Bactericidal Action Against Multidrug-Resistant Bacteria: In Vitro and In Vivo Evidence," *Colloids and Surfaces B: Biointerfaces* 217 (2022): 112688.

33. B. Koneru, Y. Shi, Y.-C. Wang, et al., "Tetracycline-Containing MCM-41 Mesoporous Silica Nanoparticles for the Treatment of Escherichia Coli," *Molecules* 20, no. 11 (2015): 19690–19698, https://doi.org/10.3390/molecules201119650.

34. A. Y. Y. Ho, E. Luong Van, C. T. Lim, et al., "Lotus Bioinspired Superhydrophobic, Self-Cleaning Surfaces From Hierarchically Assembled Templates," *Journal of Polymer Science Part B: Polymer Physics* 52 (2014): 603–609.

35. A. Jaggessar, H. Shahali, A. Mathew, and P. K. Yarlagadda, "Bio-Mimicking Nano and Micro-Structured Surface Fabrication for Antibacterial Properties in Medical Implants," *Journal of Nanobiotechnology* 15 (2017): 1–20.

36. R. Wahab, S. Ansari, Y. S. Kim, et al., "Low Temperature Solution Synthesis and Characterization of ZnO Nano-Flowers," *Materials Research Bulletin* 42, no. 9 (2007): 1640–1648, https://doi.org/10.1016/j.materresbull.2006.11.035.

37. R. Wahab, S. Ansari, Y.-S. Kim, H.-K. Seo, and H.-S. Shin, "Room Temperature Synthesis of Needle-Shaped ZnO Nanorods via Sonochemical Method," *Applied Surface Science* 253, no. 18 (2007): 7622–7626, https://doi.org/10.1016/j.apsusc.2007.03.060.

38. R. Wahab, S. Ansari, Y. S. Kim, G. Khang, and H.-S. Shin, "Effect of Hydroxylamine Hydrochloride on the Floral Decoration of Zinc Oxide Synthesized by Solution Method," *Applied Surface Science* 254 (2008): 2037–2042.

39. D. D. Thongam, J. Gupta, and N. K. Sahu, "Effect of Induced Defects on the Properties of ZnO Nanocrystals: Surfactant Role and Spectroscopic Analysis," *SN Applied Sciences* 1 (2019): 1030.

40. J. Das, S. Pradhan, D. Sahu, et al., "Micro-Raman and XPS Studies of Pure ZnO Ceramics," *Physica B: Condensed Matter* 405, no. 10 (2010): 2492–2497, https://doi.org/10.1016/j.physb.2010.03.020.

41. J. C. Fan and J. B. Goodenough, "X-Ray Photoemission Spectroscopy Studies of Sn-Doped Indium-Oxide Films," *Journal of Applied Physics* 48, no. 8 (1977): 3524–3531, https://doi.org/10.1063/1.324149.

42. R. Al-Gaashani, S. Radiman, A. R. Daud, N. Tabet, and Y. Al-Douri, "XPS and Optical Studies of Different Morphologies of ZnO Nanostructures Prepared by Microwave Methods," *Ceramics International* 39 (2013): 2283–2292.

43. H. Liao, F. Zhang, X. Liao, X. Hu, Y. Chen, and L. Deng, "Analysis of Escherichia Coli Cell Damage Induced by HPCD Using Microscopies and Fluorescent Staining," *International Journal of Food Microbiology* 144 (2010): 169–176.

44. L. Liu, K. Xu, H. Wang, et al., "Self-Assembled Cationic Peptide Nanoparticles as an Efficient Antimicrobial Agent," *Nature Nanotechnology* 4 (2009): 457–463.

45. J. D. Clogston and A. K. Patri, "Zeta Potential Measurement," in *Characterization of Nanoparticles Intended for Drug Delivery*, ed. S. E. McNeil (Humana Press, 2011), 63–70.

46. H. Wang, K. Xu, L. Liu, et al., "The Efficacy of Self-Assembled Cationic Antimicrobial Peptide Nanoparticles Against Cryptococcus Neoformans for the Treatment of Meningitis," *Biomaterials* 31 (2010): 2874–2881.

47. N. Rodrigues de Almeida, Y. Han, J. Perez, S. Kirkpatrick, Y. Wang, and M. C. Sheridan, "Design, Synthesis, and Nanostructure-Dependent Antibacterial Activity of Cationic Peptide Amphiphiles," *ACS Applied Materials & Interfaces* 11 (2019): 2790–2801.

48. C. U. Chukwudi, "rRNA Binding Sites and the Molecular Mechanism of Action of the Tetracyclines," *Antimicrobial Agents and Chemotherapy* 60 (2016): 4433–4441.

49. Z. Breijyeh, B. Jubeh, and R. Karaman, "Resistance of Gram-Negative Bacteria to Current Antibacterial Agents and Approaches to Resolve It," *Molecules* 25 (2020): 1340.

50. A. Mai-Prochnow, M. Clauson, J. Hong, and A. B. Murphy, "Gram Positive and Gram Negative Bacteria Differ in Their Sensitivity to Cold Plasma," *Scientific Reports* 6 (2016): 38610.

51. B. Gajula, S. Munnamgi, and S. Basu, "How Bacterial Biofilms Affect Chronic Wound Healing: A Narrative Review," *IJS Global Health* 3, no. 2 (2020): e16, https://doi.org/10.1097/GH9.0000000000000016.

52. H.-S. Cho, S. W. Seo, Y. M. Kim, G. Y. Jung, and J. M. Park, "Engineering Glyceraldehyde-3-Phosphate Dehydrogenase for Switching Control of Glycolysis inEscherichia Coli," *Biotechnology and Bioengineering* 109 (2012): 2612–2619.

53. Z. A. Mirani, S. Urooj, A. Ullah, et al., "Phenotypic Heterogeneity in Biofilm Consortia of E. Coli," *Microbiology* 90 (2021): 237–246.

54. C. R. Arciola, D. Campoccia, and L. Montanaro, "Detection of Biofilm-Forming Strains of Staphylococcus Epidermidis and S. Aureus," *Expert Review of Molecular Diagnostics* 2 (2002): 478–484.

55. F. Fitzpatrick, H. Humphreys, and J. P. O'Gara, "The Genetics of Staphylococcal Biofilm Formation—Will a Greater Understanding of Pathogenesis Lead to Better Management of Device-Related Infection?," *Clinical Microbiology and Infection* 11 (2005): 967–973.

56. B. Wang, Y. Yao, P. Wei, et al., "Housefly Phormicin Inhibits Staphylococcus Aureus and MRSA by Disrupting Biofilm Formation and Altering Gene Expression In Vitro and In Vivo," *International Journal of Biological Macromolecules* 167 (2021): 1424–1434.

57. H. Patel and S. Rawat, "A Genetic Regulatory See-Saw of Biofilm and Virulence in MRSA Pathogenesis," *Frontiers in Microbiology* 14 (2023): 1204428.

58. Y. Wang, Y. Feng, J. Yan, et al., "Spiky Surface Topography of Heterostructured Nanoparticles for Programmable Acceleration of Multistage Wound Healing," *Materials Today Nano* 23 (2023): 100351.

59. A. Meddahi-Pellé, A. Legrand, A. Marcellan, L. Louedec, D. Letourneur, and L. Leibler, "Organ Repair, Hemostasis, and In Vivo Bonding of

Medical Devices by Aqueous Solutions of Nanoparticles," *Angewandte Chemie International Edition* 53 (2014): 6369–6373.

60. S. Rose, A. Prevoteau, P. Elzière, D. Hourdet, A. Marcellan, and L. Leibler, "Nanoparticle Solutions as Adhesives for Gels and Biological Tissues," *Nature* 505 (2014): 382–385.

61. V. Lakshmi Prasanna and R. Vijayaraghavan, "Insight Into the Mechanism of Antibacterial Activity of ZnO: Surface Defects Mediated Reactive Oxygen Species Even in the Dark," *Langmuir* 31 (2015): 9155–9162.

62. A. Happy, M. Soumya, S. Venkat Kumar, and S. Rajeshkumar, "Mechanistic Study on Antibacterial Action of Zinc Oxide Nanoparticles Synthesized Using Green Route," *Chemico-Biological Interactions* 286 (2018): 60–70.

63. Y. Xia, X. Fan, H. Yang, et al., "ZnO/Nanocarbons-Modified Fibrous Scaffolds for Stem Cell-Based Osteogenic Differentiation," *Small* 16 (2020): 2003010.

64. A. Dodero, S. Scarfi, M. Pozzolini, S. Vicini, M. Alloisio, and M. Castellano, "Alginate-Based Electrospun Membranes Containing ZnO Nanoparticles as Potential Wound Healing Patches: Biological, Mechanical, and Physicochemical Characterization," *ACS Applied Materials & Interfaces* 12 (2020): 3371–3381.

65. Y. Hedberg, X. Wang, J. Hedberg, M. Lundin, E. Blomberg, and I. Odnevall Wallinder, "Surface-Protein Interactions on Different Stainless Steel Grades: Effects of Protein Adsorption, Surface Changes and Metal Release," *Journal of Materials Science: Materials in Medicine* 24, no. 4 (2013): 1015–1033, https://doi.org/10.1007/s10856-013-4859-8.

66. Z. Wen, X. Shi, X. Li, et al., "Mesoporous TiO2Coatings Regulate ZnO Nanoparticle Loading and Zn2+Release on Titanium Dental Implants for Sustained Osteogenic and Antibacterial Activity," *ACS Applied Materials & Interfaces* 15 (2023): 15235–15249.

Supporting Information

Additional supporting information can be found online in the Supporting Information section.